Applied Physics Letters ARTICLE scitation.org/journal/apl

HZO-based FerroNEMS MAC for in-memory computing

Cite as: Appl. Phys. Lett. **121**, 193503 (2022); doi: 10.1063/5.0120629
Submitted: 13 August 2022 · Accepted: 27 October 2022 ·
Published Online: 11 November 2022

View Online

Export Citation

CrossMark

Shubham Jadhav,[1,a)] Ved Gund,[1] Benyamin Davaji,[1,3] Debdeep Jena,[1,2] Huili (Grace) Xing,[1,2] and Amit Lal[1]

AFFILIATIONS

[1]School of Electrical and Computer Engineering, Cornell University, Ithaca, New York 14853, USA
[2]Department of Materials Science and Engineering, Cornell University, Ithaca, New York 14853, USA
[3]Electrical and Computer Engineering Department, Northeastern University, Boston, Massachusetts 02115, USA

[a)]Author to whom correspondence should be addressed: saj96@cornell.edu

ABSTRACT

This paper demonstrates a hafnium zirconium oxide (HZO)-based ferroelectric NEMS unimorph as the fundamental building block for very low-energy capacitive readout in-memory computing. The reported device consists of a $250 \times 30\ \mu m^2$ unimorph cantilever with 20-nm-thick ferroelectric HZO on $1\ \mu m$ SiO_2. Partial ferroelectric switching in HZO achieves analog programmable control of the piezoelectric coefficient (d_{31}), which serves as the computational weight for multiply accumulate (MAC) operations. The displacement of the piezoelectric unimorph was recorded by actuating the device with different input voltages V_{in}. The resulting displacement was measured as a function of the ferroelectric programming/poling voltage V_P. The slopes of central beam displacement (δ_{max}) vs V_{in} were measured to be between 182.9 nm/V (for $-8\ V_p$) and -90.5 nm/V (for $8\ V_p$), which corresponds to displacement proportionality constant β of 68 nm/V^2 for +ve V_p and 47 nm/V^2 for −ve V_p, demonstrating linear behavior of the multiplier unit. The resultant δ_{max} from AC actuation is in the range of −18 to 36 nm and is a scaled product of V_{in} and programmed d_{31} (governed by the V_p). The multiplication function serves as the fundamental unit for MAC operations with the ferroelectric NEMS unimorph. The displacement from many such beams can be added by summing the capacitance changes, providing a pathway to implement a multi-input and multi-weight neuron. A scaling and fabrication analysis suggests that this device can be CMOS compatible, achieving high in-memory computational throughput.

Published under an exclusive license by AIP Publishing. https://doi.org/10.1063/5.0120629

Neuromorphic computation is of great interest to computing theory and practical implementations due to the potential for low-power, high efficiency, and small form factor information processing with deep neural networks (DNNs).[1–3] The building blocks of DNNs are perceptron blocks, which inherently necessitate brain-like synaptic functions achieved through arrays of multiply accumulate (MAC) units. With the ever-increasing number of variables required for neuromorphic computation with high accuracy, there is an urgent need to develop highly energy-efficient device architectures.[3–5] The energy used per MAC unit is, therefore, a useful metric to compare technologies. Ferroelectric field-effect transistors (Fe-FET) have been used to mimic analog synaptic operation with gate-ferroelectric switching in silicon and germanium channel devices to realize multi-level conductance modulation with potentiation and depression with 50–100 ns switching pulses and 3–5 MV/cm fields.[6,7] FET-based in-memory computation architectures are susceptible to large read and write energy consumption and high leakage currents in idle mode, particularly with gate dielectric thickness scaling down to <5 nm.[8] Resistive random access memory (RRAM) enables neuromorphic synaptic functionality but necessitates current-based control circuitry that can limit the dynamic range and the effective number of bits. Nano Electro-Mechanical Systems (NEMS) switches and beams offer an alternate pathway to zero-leakage in-memory compute synaptic functionality, provided that the beam actuation has embedded programmable weights in the form of tunable capacitive or piezoelectric coupling. Such switches are especially useful where infrequent update of neuromorphic weights is needed and the analog programming can be done at DC or low frequencies. We have previously reported a graphene-on-HZO ferroelectric device that uses potential gradients across the graphene to achieve fractional switching, with the modulated graphene resistance also used for resistive memory readout.[9] While analog in-memory computing has been demonstrated using different architectures that use transistors or memristors, few prior works have used an NEMS-based approach that takes advantage of a released beam structure to eliminate energy leakage in an idle state.[10–13] In previous work, the idea of using nanomechanical electrostatic actuators to

Published under an exclusive license by AIP Publishing

produce MAC units has been described.[13] In contrast, we present a ferroelectric/piezoelectric beam transducer to enable the multiplication that can be readout capacitively, eliminating any DC currents.

This paper presents a technique to store the neural net weights in the form of the programmable piezoelectric coefficient d_{31} of an HZO-driven unimorph. Similar to a fixed–free unimorph, the fixed–fixed unimorph displacement is proportional to d_{31}.[14] The d_{31} is modulated by applying a polarization switching voltage V_p. After polarization programming, different actuation inputs (V_{in}) actuate the cantilever such that the unimorph displacement is a scaled product of V_p and V_{in}. The displacement can in turn be measured as capacitive sense current from a capacitive divider circuit, for massively parallel MAC operations from arrays of such NEMS elements. Figure 1 shows the concept of the partial polarization in a ferroelectric for analog control of beam-bending in a unimorph. In addition to the active ferroelectric film, the unimorph stack also includes metal contact layers and an insulating elastic layer. The polarization vs E-field (PE loop) for an 80 μm diameter metal–ferroelectric–metal (MFM) capacitor on a 20-nm-thin HZO film is shown in Fig. 1(a). Moving counterclockwise along the PE loop starting with all dipoles point downward (point O), the film can be in a state of net-zero polarization (points A and A′) at the positive and negative coercive fields, fully down- or up-switched (points C and C′) or partially polarized (along the slopes of A–B and A′–B′). Each point along the PE loop achieves a specific macroscopic value of d_{31}, with the maximum and minimum values at the two extrema (at points C and C′) using the appropriate choice of poling voltage $V_p = E_p t_{HZO}$. After programming, if a much smaller actuation voltage V_{in} is applied such that it produces no dipole switching, an in-plane stress is generated due to expansion or contraction of the HZO film along its length, resulting in the piezoelectric bending moment M_{Piezo}. The programming would enable weight-storage in DNNs at reduced rates compared to inference events.

For a given V_P and V_{in}, the NEMS beam displacement is, a scaled product of weights and inputs (detailed derivation in the supplementary material, Sec. IA)

$$\delta_{\max} = \beta \cdot V_p \cdot V_{in}. \tag{1}$$

Here, β is the displacement proportionality constant that depends on ferroelectric material properties, beam geometry, Young's modulus, etc. We can design the multiplier to achieve linear behavior in the transfer characteristics curve along the rising and falling slopes of the PE loop to accomplish a multiplicative function for parallel MAC operations. Figure 1(c) represents the multiplier unit with a capacitive readout to measure the output voltage. The left and right beams are poled with the same voltage amplitude but opposite polarity. Thus, for the same input voltage V_{in}, the left and right beams displace such that the difference between the two represents the product of V_{in} and V_P. The differential motion causes differential capacitance between left and right capacitive parallel plates. The output voltage is given by

$$V_{out} = V_{dd}\frac{C_L - C_R}{C_L + C_R} \cong V_{dd}\gamma\frac{\delta_{\max,L} - \delta_{\max,R}}{2g} = SF \cdot V_p \cdot V_{in}. \tag{2}$$

Here, $\delta_{max,L}$ and $\delta_{max,R}$ are left and right beam center displacements with initial gap g. γ is an constant, which relates δ_{max} to the parallel plate displacement at sense electrode (see the supplementary material, Sec. IA, for detailed derivation). Several multiplier units can then be

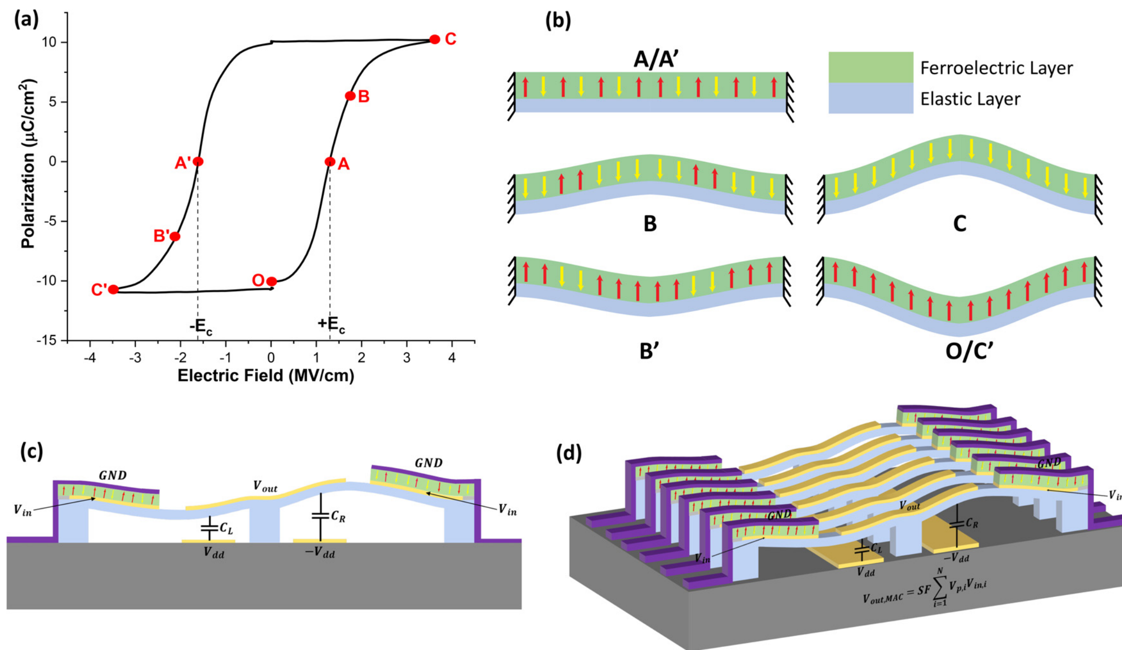

FIG. 1. (a) PUND loop of 20-nm-thick HZO film. (b) Polarization-dependent bending moment generated in ferroelectric-on-elastic unimorph at various points along the PE loop (E_C is coercive field). (c) Schematic for multiplier unit with ferroelectric actuation and capacitive readout. The output voltage is the product of V_{in} and stored weights in the form of d_{31} coefficients. (d) Several multipliers with capacitive readout can be placed in parallel to form a MAC unit that can perform accumulation operation by summing up the capacitances from each device.

Published under an exclusive license by AIP Publishing

further connected in parallel with an activation unit to form a perceptron. The output voltage of the MAC unit [Fig. 1(d)] is

$$V_{out,MAC} = V_{dd}\frac{\sum_{i=1}^{N} C_{L,i} - \sum_{i=1}^{N} C_{R,i}}{\sum_{i=1}^{N} C_{L,i} + \sum_{i=1}^{N} C_{R,i}} = SF\sum_{i=1}^{N} V_{p,i}\cdot V_{in,i}. \quad (3)$$

Figures 2(a) and 2(b) show the top and cross section views, respectively, of the clamped–clamped ferroelectric unimorph used to demonstrate piezoelectric coefficient programming. 1-μm-thick thermal SiO_2 forms the elastic layer underneath 20 nm ferroelectric HZO. The HZO is capped by 3 nm of alumina (Al_2O_3), followed by annealing at 400 °C to crystallize the HZO in its ferroelectric orthorhombic phase. 200 nm platinum (Pt) and 100 nm aluminum (Al) were deposited to form the bottom and top metal contacts for the HZO, respectively. The beam was released by isotropic etching of the silicon substrate using Xactix XeF_2 etcher (full process flow shown in the supplementary material, Sec. II). A scanning electron microscope image of the fabricated device is shown in Fig. 2(c). After release, the beams were observed to be buckled due to residual film-stress generated during microfabrication. A 3D optical profilometer (Zygo^{TM} system) was used to measure the beam buckling profile [Fig. 2(d)]. The observed center-buckling for a $250 \times 30\,\mu m^2$ was 4.98 μm.

HZO ferroelectric characterization was performed using a Sawyer–Tower circuit configuration on a custom probe station with continuous wave (CW) positive-up-negative-down (PUND) input waveforms to extract the coercive field (E_C) and remnant polarization (P_r). In prior work, we have used electrical breakdown under a large top metal pad to contact the bottom electrode with 5–10 Ω resistance.[15] The PUND input signal has 83 μs rise, fall, and wait times (corresponding to 1 kHz PUND frequency), and a peak-to-peak amplitude of 15 V. Figure 3(a) shows time-domain input voltage and output sense current measured with an 11.8 kΩ sense resistor. The P and N pulses show a switching current peak below the peak voltage, indicative of polarization switching, whereas the U and D pulses show capacitive displacement current and low leakage. This confirms ferroelectricity in the released HZO films without any degradation, consistent over more than 10 000 cycles of switching with CW operation. Figure 3(b) plots the switching current density (J) vs E-field. The PUND measurement was performed on multiple such released NEMS beams with a range of lengths from 100 to 400 μm and widths spanning 15–39 μm. The overlay from these measurements is shown with multiple dotted lines in Fig. 3(c). For comparison, the PUND loop for an unreleased 80 μm diameter circular electrode is also shown on the same plot (solid black line). This shows that there is little/no degradation of ferroelectric properties of the HZO before and after release; P_r is unchanged and E_C has a small increase in ∼14%, a likely result of the reduced slope-steepness of the PE curve, due to stress relief in released devices. Multiple release devices with different electrode sizes show overlapping loops suggesting high repeatability. PUND measurements yield an extracted $E_c \approx 1.5$ MV/cm and $P_r \approx 10\,\mu C/cm^2$, consistent with previously reported values.[16–20] The devices were also tested for DC breakdown as shown in Fig. 3(d). The device's current density exceeds 10 $\mu A/cm^2$ at 3.15 MV/cm.

The central concept of this work is to use analog weight storage in the bending motion of the NEMS beam for in-memory computation, which relies on the programming of the d_{31} coefficient of the device by using different poling voltages. The test methodology used for this experiment is as follows:

Step 1: Device poling with CW single-sided pulses at 3 kHz. The configuration used for poling is depicted in Fig. 3(a) (inset). The test signal is applied to the top electrode, and the ground

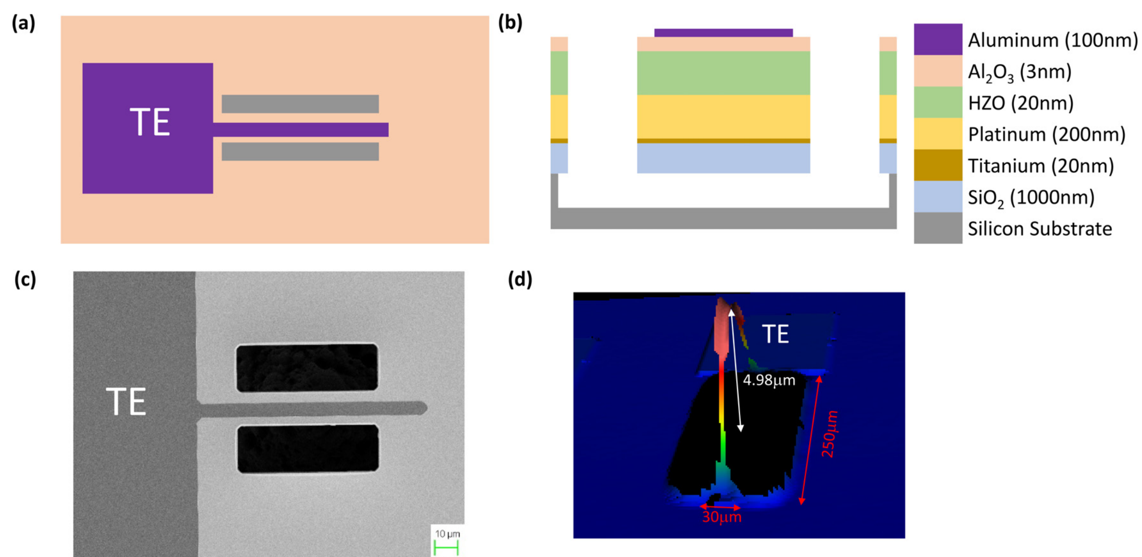

FIG. 2. (a) Schematic top and (b) cross-sectional view of the ferroelectric beam. (c) Scanning electron microscopy (SEM) image of the beam showing released structure. (d) 3D profile of the released beam measured using Zygo^{TM} profilometer showing beam curvature due to residual stresses in the stack. For $250 \times 30\,\mu m^2$ beam, the measured maximum displacement at the center was 4.98 μm.

Published under an exclusive license by AIP Publishing

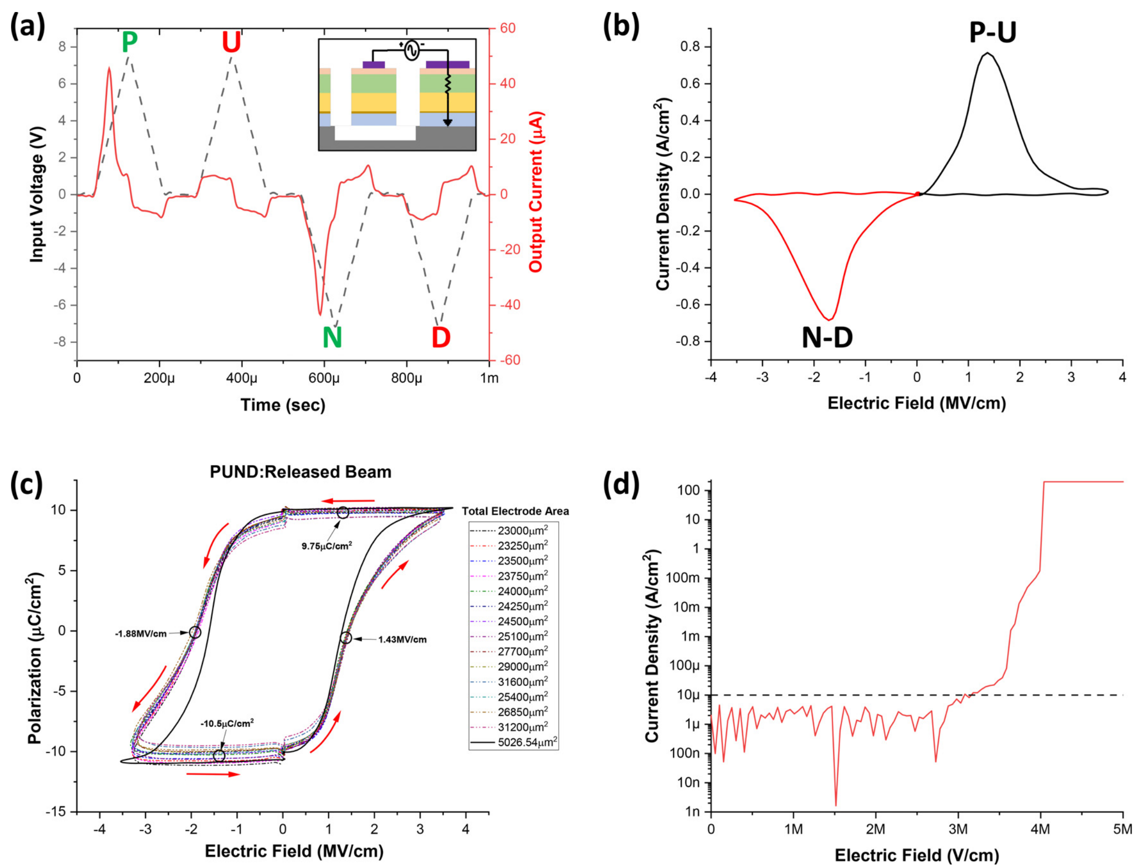

FIG. 3. (a) Plot of input voltage and output current over 1 PUND cycle showing much larger switching currents as compared to leakage currents. (Inset) Configuration for poling the NEMS beam. (b) Switching-current density (J) vs electric field (E) showing ferroelectric switching peaks. (c) Measured PE characteristics of released beam devices with different lengths and widths showing repeatability. The measured PE loop of the standard unreleased circular electrode is shown with a solid black line. (d) DC-IV of the device showing high current density above 3.15 MV/cm indicating leakage.

connection is made to the bottom electrode by breaking down the HZO under a large top metal pad to short it to the bottom electrode.

Step 2: Beam actuation with a small V_{in} to measure the displacement amplitude, without additional polarization switching.

Step 3: Increase poling voltage by 0.5 V and repeat steps 1–2, while tracing the PE loop counterclockwise from 0 V → 8 V → 0 V → −8 V → 0 V.

This voltage sweep for V_p is similar to the PUND loop with one key difference. In this technique, we stepped the V_p by 0.5 V and then measured the beam displacement with a fixed V_{in} amplitude, unlike the PUND measurements in CW operation with increasing voltages.

A Polytec MSA-400 laser Doppler vibrometer (LDV) was used to measure the beam motion. For a 250 × 30 μm^2 beam, a 0.1 V amplitude frequency chirp from 1 kHz to 1 MHz was applied. A resonance at $f_0 = 455.23$ kHz was identified with a quality factor of Q = 305. After each poling, AC voltage V_{in}=0.1 V was used to actuate and measure amplified beam displacement at f_0, to achieve improved displacement resolution compared to low-frequency or DC actuation. Figure 4(a) shows the peak beam displacement δ_{max} and resonant frequency f_0 vs poling voltage V_p plot for the nominal 250 × 30 μm^2 ferroelectric clamped–clamped beam. δ_{max} (red line) is modulated for different values of V_p and traces a hysteresis loop, similar to the PE loop from PUND measurements. The net effect of the number of upward and downward pointing dipoles that control the macroscopic polarization in the beam (induced due to V_p) also changes the beam stiffness resulting in resonance frequency modulation (black line), which presents a separate modality of weight storage in the beam. The two dips in f_0 correspond to the positive and negative coercive fields of the HZO film, where the net polarization is almost zero. As illustrated in Fig. 1(b), domain randomization is a potential cause for likely film relaxation at these points causing f_0 to drop.

From Fig. 4(a), the positive linear dependence of δ_{max} can be seen in the voltage interval 2.5 V → 8 V (rising slope). Similarly, negative linear dependence in the interval −2.5 V → −8 V (falling slope). Here, the slope of δ_{max} vs V_p for constant V_{in} is β as defined in Eq. (1). The effect of V_{in} on δ_{max} is explained in paragraph. Two points were selected on the positive slope to show the resonance vibration magnitude and phase plots of the vibrating beam [Fig. 4(b)]. Points 1 and 2 have nearly the same displacement magnitude but exactly opposite phases. This 180° phase difference is a signature of polarization

Published under an exclusive license by AIP Publishing

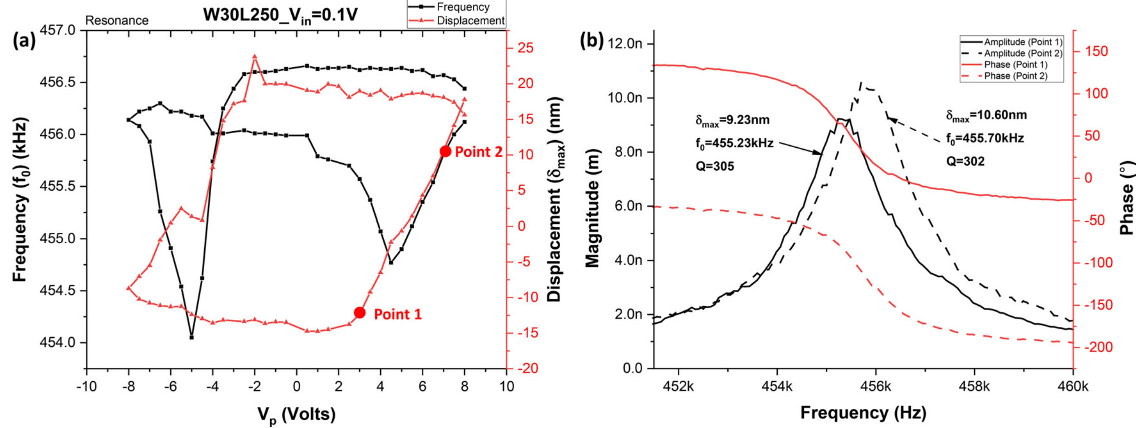

FIG. 4. (a) Central beam displacement δ_{max} and resonant frequency f_0 vs poling voltage V_p plot for the $250 \times 30\,\mu m^2$ ferroelectric clamped–clamped beam. Devices were poled at different V_p with 0.5 V increment along the loop (0 V → 8 V → 0 V → 8 V → 0 V), and the beam displacement profile was measured using the Polytec laser Doppler vibrometer (LDV) at $V_{in} = 0.1$ V in the frequency range of 450–460 kHz. The δ_{max} (red line) changes for different values of V_p and traces a hysteresis loop similar to PUND measurements. The polarization in the beam, induced due to V_p, changes the internal stress resulting in the frequency f_0 tuning (black line) which could be exploited for memory storage. (b) The resonance vibration magnitude and phase plots of the same beam at different points on plot (a).

inversion corresponding to a sign change for δ_{max}. To show the effect of V_{in} on δ_{max}, V_{in} was swept from 0.02 to 0.20 V for different values of the V_p [Fig. 5(a)].

Figure 5(a) plots δ_{max} vs V_{in} at different values of V_p, which emulates the transfer characteristics of the analog multiplier. For a fixed poling voltage, an input voltage sweep yields a linear increase in displacement value. Similarly, for constant inputs, different poling voltages outputs different displacement values. The slope of the plot in Fig. 5(a) is the experimental $\beta \times V_p$. We can calculate the displacement proportionality constant β from Fig. 5(a) as follows:

$$\beta = \frac{\delta_{max}}{V_p\, V_{in}}. \tag{4}$$

Figure 5(b) shows that the experimentally measured values of β in the positive (rising edge of PE) and negative (falling edge of PE) regions are 68 and 47 nm/V^2, respectively. Both values are relatively constant over the range of ± 5.5 to ± 8 V V_p. Thus, our assumption of constant β and in turn constant SF holds true. An asymmetry of the electrodes (Al on top and Pt on bottom) as well as the presence of any non-switchable polarization in the material is likely the reason for difference in the negative and positive β value.[21] Thus, for the same V_p, actuation with opposite polarity will have an unequal effect on the partial polarization resulting in different δ_{max} values. This inequality can be mitigated by scaling V_p accordingly (see the supplementary material, Sec. IB, for more details). Equation (4) demonstrates that δ_{max} is the scaled product of inputs (V_{in}) and weights (V_p). This is a linear equation in the range of ± 2.5 to ± 8 V V_p and 0 to 0.2 V V_{in} for the device tested here ($250 \times 30\,\mu m^2$ beam).

In conclusion, we have demonstrated the working of an HZO-based NEMS multiplier with weight storage functionality. The device was fabricated and tested to prove the dependence of beam displacement on the poling voltage of the ferroelectric film. Polarization-dependent

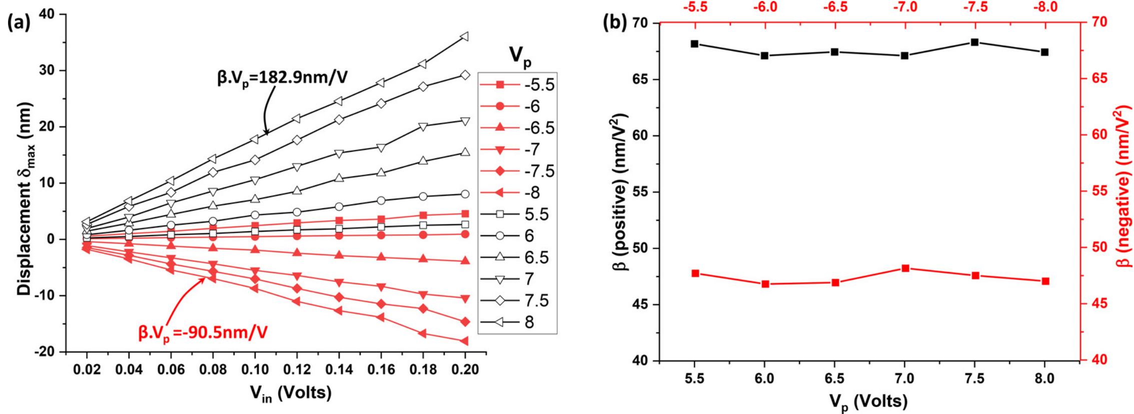

FIG. 5. (a) The displacement vs V_{in} for different values of V_p. The black and red traces correspond to the positive V_p (5.5 → 8 V) and negative V_p (−5.5 → −8 V), respectively, showing the multiplication functionality. (b) β vs V_p plot for positive (black) and negative (red) V_p showing constant β over the range of ± 5.5 to ± 8 V V_p.

Published under an exclusive license by AIP Publishing

frequency-tuning was also observed, which can be further explored to achieve an electrically reconfigurable filter. For a $250 \times 30\,\mu m^2$ beam poled at 8 V, $\delta_{max} = 18$ nm and $f_0 = 455.23$ kHz was measured with a Q = 305. The δ_{max} vs V_{in} plot at different values of V_p demonstrate the operation of an analog NEMS multiplier. While this study uses AC actuation of the beam, in the future, DC input voltages are anticipated for DNN applications. A capacitive readout of the beam motion can be used instead of a topical readout for much higher resolution [as illustrated in Fig. 1(c)].

The dimensional and voltage scaling of the prototype device demonstrated is critical for CMOS-integrated adoption while maximizing computational throughput. For CMOS compatibility, <1 V operation is necessary. This sets an upper bound for HZO film thickness of <7 nm for $E_C = 1.5$ MV/cm. Non-resonant actuation of the devices would require a settling time of $\sim 2QT_0$. Assuming two operations per device, multiplication and addition, the computation speed (FLOPS per device) and power consumption can be estimated as $\frac{f_0}{Q}$ and E$\frac{f_0}{Q}$, respectively. Here, E is the energy consumption per operation for an individual device given by $\frac{1}{2}C_{HZO}.V_{in}^2$. For example, a unimorph device of size $5 \times 0.5\,\mu m^2$ and thickness 28 nm ($\sim 4\times$ HZO thickness) with a Q = 10, which can be realized by high-pressure gas damping, yields f_0 ~20 MHz and computation speed of 2 MFLOPS/device. Considering driving electrodes of size 1×0.3 μm with 7-nm-thick HZO between V_{in} (0.1 V) and GND electrodes, the energy consumption per operation can be calculated as ~500 aJ $\left(E = \frac{1}{2}C_{HZO} \cdot V_{in}^2\right)$. Combining both values results in 2 PFLOPS/watt computational performance. This computation speed with ultra-low energy consumption and zero leakage current will pave the path toward brain-level computation efficiency.

See the supplementary material for further details.

This work was performed in part at the Cornell NanoScale Facility, an NNCI member supported by NSF Grant No. NNCI-2025233. Funding was provided by the DARPA TUFEN (No. HR0011-20-9-0048) program.

AUTHOR DECLARATIONS

Conflict of Interest

The authors have no conflicts to disclose.

Author Contributions

Shubham Avinash Jadhav: Conceptualization (equal); Data curation (lead); Formal analysis (equal); Methodology (lead); Visualization (lead); Writing – original draft (equal); Writing – review & editing (equal). **Ved Gund:** Conceptualization (equal); Data curation (supporting); Formal analysis (equal); Methodology (supporting); Supervision (supporting); Visualization (supporting); Writing – review & editing (equal). **Benyamin Davaji:** Conceptualization (supporting); Methodology (supporting); Supervision (supporting). **Debdeep Jena:** Conceptualization (supporting); Data curation (supporting); Funding acquisition (equal); Project administration (equal); Supervision (supporting). **Huili Grace Xing:** Conceptualization (supporting); Funding acquisition (equal); Project administration (equal). **Amit Lal:** Conceptualization (lead); Data curation (equal); Formal analysis (equal); Funding acquisition (equal); Investigation (lead); Project administration (lead); Resources (lead); Supervision (lead); Visualization (supporting); Writing – review & editing (equal).

DATA AVAILABILITY

The data that support the findings of this study are available from the corresponding author upon reasonable request.

REFERENCES

[1] C. Mead, Proc. IEEE **78**, 1629 (1990).
[2] E. R. Kandel, T. M. Jessell, J. H. Schwartz, S. A. Siegelbaum, and A. J. Hudspeth, *Principles of Neural Science,* 5th edition (McGraw Hill Professional, 2013).
[3] A. Keshavarzi, K. Ni, W. Van Den Hoek, S. Datta, and A. Raychowdhury, IEEE Micro **40**, 33 (2020).
[4] W. Haensch, T. Gokmen, and R. Puri, Proc. IEEE **107**, 108 (2019).
[5] M. Horowitz, 10 (2014).
[6] M. Si, X. Lyu, and P. D. Ye, ACS Appl. Electron. Mater. **1**, 745 (2019).
[7] M. Jerry, P.-Y. Chen, J. Zhang, P. Sharma, K. Ni, S. Yu, and S. Datta, in IEEE International Electron Devices Meeting (IEEE, 2017), pp. 6.2.1–6.2.4.
[8] S. S. Cheema, D. Kwon, N. Shanker, R. dos Reis, S.-L. Hsu, J. Xiao, H. Zhang, R. Wagner, A. Datar, M. R. McCarter, C. R. Serrao, A. K. Yadav, G. Karbasian, C.-H. Hsu, A. J. Tan, L.-C. Wang, V. Thakare, X. Zhang, A. Mehta, E. Karapetrova, R. V. Chopdekar, P. Shafer, E. Arenholz, C. Hu, R. Proksch, R. Ramesh, J. Ciston, and S. Salahuddin, Nature **580**, 478 (2020).
[9] V. Gund, B. Davaji, S. Jadhav, H. Lee, H. G. Xing, D. Jena, and A. Lal, in IEEE International Frequency Control Symposium, 2022.
[10] A. Chen, S. Datta, X. S. Hu, M. T. Niemier, T. Š. Rosing, and J. J. Yang, IEEE Des. Test **36**, 46 (2019).
[11] A. Sebastian, M. L. Gallo, R. Khaddam-Aljameh, and E. Eleftheriou, Nat. Nanotechnol. **15**, 529 (2020).
[12] D. E. Nikonov and I. A. Young, IEEE J. Explor. Solid-State Comput. Devices Circuits **5**, 75 (2019).
[13] A. Lal, J. Hoople, S. Ardanuç, and J. Kuo, "Neurons based on nanoelectromechanical systems," U.S. Patent No. US10860916B2 (8 December 2018); available online at https://patents.google.com/patent/US10860916B2/en.
[14] Q. M. Wang, X. H. Du, B. Xu, and L. E. Cross, IEEE Trans. Ultrason. Ferroelectr, Freq. Control **46**, 638 (1999).
[15] V. Gund, B. Davaji, H. Lee, M. J. Asadi, J. Casamento, H. G. Xing, D. Jena, and A. Lal, in *IEEE International Symposium on Applications of Ferroelectrics* (IEEE, 2021), pp. 1–3.
[16] J. Müller, T. S. Böscke, D. Bräuhaus, U. Schröder, U. Böttger, J. Sundqvist, P. Kcher, T. Mikolajick, and L. Frey, Appl. Phys. Lett. **99**, 112901 (2011).
[17] M. Hyuk Park, H. Joon Kim, Y. Jin Kim, W. Lee, T. Moon, and C. S. Hwang, Appl. Phys. Lett. **102**, 242905 (2013).
[18] S. Starschich, T. Schenk, U. Schroeder, and U. Boettger, Appl. Phys. Lett. **110**, 182905 (2017).
[19] J. Muller, T. S. Boscke, S. Muller, E. Yurchuk, P. Polakowski, J. Paul, D. Martin, T. Schenk, K. Khullar, A. Kersch, W. Weinreich, S. Riedel, K. Seidel, A. Kumar, T. M. Arruda, S. V. Kalinin, T. Schlosser, R. Boschke, R. Van Bentum, U. Schroder, and T. Mikolajick, in International Electron Devices Meeting (IEDM), 2013.
[20] M. Ghatge, G. Walters, T. Nishida, and R. Tabrizian, in International Electron Devices Meeting (IEDM), 2019.
[21] I. Stolichnov, M. Cavalieri, E. Colla, T. Schenk, T. Mittmann, T. Mikolajick, U. Schroeder, and A. M. Ionescu, ACS Appl. Mater. Interfaces **10**, 30514 (2018).

Published under an exclusive license by AIP Publishing